The effect of local ventilation on a spatiotemporal model of airborne disease transmission in indoor spaces.

Alexander Pretty[1], Ian M. Griffiths[2], Zechariah Lau[1,2] and Katerina Kaouri[1]

[1]School of Mathematics, Cardiff University, Cardiff, CF24 4AG, UK

[2]Mathematical Institute, University of Oxford, Oxford, OX2 6GG, UK

Corresponding email: prettya@cardiff.ac.uk

Received: XX XX XX; **Revised:** XX XX XX; **Accepted:** XX XX XX

Key words: Epidemiology, Diffusion and convection, Mathematical modeling or simulation for problems pertaining to fluid mechanics, Reaction-diffusion equations

Abstract

We incorporate local ventilation effects into a spatially dependent generalisation of the Wells–Riley model for airborne disease transmission (Lau *et al.*, 2022) and consider a room in which an air purifier supplements the ventilation provided by a poorly functioning air-conditioning unit. Aerosol production and removal through ventilation, biological deactivation, and gravitational settling as well as transport around a recirculating air-conditioning flow and global turbulent mixing are modelled using an advection–diffusion–reaction equation. This local ventilation model is compared with a global ventilation model, where all ventilation is treated as a global sink. We undertake this comparison for a weak purifier (Clean Air Delivery Rate of 140 m^3h^{-1}) and a strong purifier (Clean Air Delivery Rate of 1,000 m^3h^{-1}). For each purifier, we determine a total effective air exchange rate and compare against the global model with equivalent ventilation.

We find that, as expected, the purifier removes fewer aerosols when the distance between the infectious person and the purifier is increased, resulting in a greater average aerosol concentration in the room. Moreover, the concentration is generally lowest when the infectious person is upstream of the purifier, located in regions where the airflow streamlines are directed into the purifier. For these infectious source locations, the global ventilation model significantly overestimates the concentration throughout the room. For infectious sources outside of these regions, there is generally good agreement between the models, particularly for the weak purifier.

We also studied, for a fixed distance from the purifier, how the infection risk to a susceptible person varies as the infectious person changes location. A susceptible person faces the highest infection risk when they are directly downstream of the infectious person, where the aerosol concentration is the highest. There is better agreement between local and global ventilation models for the weak purifier than for the strong purifier since the weak purifier has less impact on the airflow in the room.

1. Introduction

The importance of ventilation in reducing the indoor transmission of infectious diseases was first highlighted by Nightingale (1860). When an infectious person breathes, talks, coughs, or sneezes, disease-carrying particles are emitted. In poorly ventilated spaces, small particles known as *aerosols* can remain airborne for several hours, transmitting

the disease to susceptible people when inhaled. During the COVID-19 pandemic, a key shift in understanding and mitigating transmission of the SARS-CoV-2 virus was the recognition of airborne transmission (Morawska & Milton, 2020), most likely responsible for superspreader outbreaks in a restaurant (Lu, 2020; Ho, 2021), courtroom (Vernez *et al.*, 2021), choir practice (Miller, 2021), and meat processing plant (Günther, 2020).

There are two main approaches to modelling airborne transmission: Wells–Riley models and Computational Fluid Dynamics (CFD). Wells–Riley models (Riley *et al.*, 1978) assume a well-mixed room, meaning aerosols are instantaneously transported throughout the room. Due to its high computational speed, this approach can be readily applied throughout an epidemic; this was the case for COVID-19 (Buonanno *et al.*, 2020; Dai & Zhao, 2020; Lelieveld, 2020). However, the well-mixed-room assumption is not always appropriate and neglects the spatial variation of the concentration around the room. One benefit of this approach is its broad applicability – results do not depend on the specific configuration of people, furniture, and ventilation.

CFD models, on the other hand, simulate the detailed airflow in a room with a specific layout. The computational demand is high, so many CFD studies at the start of the COVID-19 pandemic focused on relatively short time frames (less than 5 minutes) (Shafaghi *et al.*, 2020; Vuorinen, 2020). This simulation time is appropriate for heavier virus-laden droplets that quickly fall to the ground, but untenable for airborne transmission, which typically occurs over hours. Some CFD models have simulated aerosol evolution for up to an hour (Shao *et al.*, 2021), but the high computational times means that CFD has a limited role in informing up-to-date decisions in a quickly developing epidemic. One key advantage of CFD models is in exploring a transmission event after-the-fact (Ho, 2021) to better understand the mechanisms influencing transmission.

Lau *et al.* (2022) model the spatiotemporal evolution of aerosols in a room using an advection–diffusion–reaction (ADR) equation under the assumption of a recirculating airflow generated by an air-conditioning (AC) vent. Extending the Wells–Riley model, the Lau *et al.* (2022) model accounts for the spatial variation of concentration and infection risk. Moreover, the airflow can be reduced to a 2D flow, which allows fast simulations, so the model can be quickly deployed in a fast-changing epidemic. Aerosol removal by ventilation is modelled as a global sink, as in the Wells–Riley type models. Under this assumption, good agreement with real-life scenarios ventilated by inbuilt AC units was obtained (Lau *et al.*, 2022).

For rooms with poor or non-existent ventilation, air purifiers can increase overall aerosol removal. The effectiveness of air purifiers depends strongly on their location (Burgmann & Janoske, 2021; Narayanan & Yang, 2021), an effect that cannot be captured by the Wells–Riley model or the model of Lau *et al.* (2022). Moreover, many CFD studies of air purifiers report prohibitively long computational times; for example Dbouk *et al.* (2021) report 7 days to simulate a 2.5-minute event in a domestic setting. While air purifiers are not technically classified as ventilation, since they do not provide fresh air from outdoors, the American Society of Heating, Refrigeration and Air-Conditioning (ASHRAE) incorporate air cleaning devices in their measure of *equivalent clean airflow* when risk of disease transmission is high (e.g. during an epidemic) (ASHRAE, 2023). In the present study, following ASHRAE, we conflate air purifiers with ventilation since we are solely interested in aerosol removal. However, we note that relying only on air purifiers with no outdoor air exchange can result in a build up of carbon dioxide, degrading the indoor air quality. The efficacy of an air purifier is described by the Clean Air Delivery Rate (CADR) which is a combination of the filter efficacy and the volumetric flow-rate through the device.

In this paper, we introduce spatially localised ventilation to the modelling framework of Lau *et al.* (2022). While all ventilation systems (including doors, windows and AC units)

have local effects, we are motivated by air purifiers; we introduce a cylindrical device that draws air in through the top and expels clean air from the bottom. This device is placed in addition to an inbuilt, poorly performing, AC unit.

The model allows quick investigation of transmission events over long periods of time. Lectures, meetings, school lessons, and certain time-limited social events (e.g. escape rooms) usually last for about an hour. Significantly more time is spent in restaurants, art galleries, networking events (e.g. conferences and workshops), and other social settings (e.g. pub quizzes). These scenarios are common transmission events for airborne diseases. We consider 1- and 4-hour events to explore the effectiveness of air purifiers in such settings.

The paper is organised as follows. The modelling framework, incorporating a local ventilation system, is presented in §2. In §3, we compare the average aerosol concentration in the room predicted by the local and global ventilation models. The spatial distribution of aerosols is then compared in §4. In §5, we compare the infection risk at specific locations arising from the two ventilation models. Conclusions and suggestions for future work are provided in §6.

2. Modelling framework

2.1. Global ventilation models

Prior to detailing the modelling framework of the present study, a brief overview of two pertinent models is provided. First, we describe the Wells–Riley model. The spatiotemporal generalisation of this model implemented by Lau *et al.* (2022) is then described.

The Wells–Riley model and its variants (Gammaitoni & Nucci, 1997; Miller, 2021) assume a well-mixed room, meaning the aerosol concentration is spatially uniform and depends only on time, t. The aerosol concentration in the room, $C(t)$, is thus governed by the ODE

$$\frac{\mathrm{d}C}{\mathrm{d}t} = \frac{R}{V} - (\lambda + \beta + \sigma)C. \tag{2.1}$$

This closely matches the formulation used by Miller (2021). The first term on the right-hand side describes aerosol production as a global source, with R denoting the rate at which aerosols are produced and V being the room volume. The second term on the right-hand side describes first-order removal of aerosols through a global sink, where each coefficient is the rate at which aerosols are removed by ventilation (λ), biological deactivation (β), and gravitational settling (σ).

In addition to (2.1), Wells–Riley models relate the aerosol concentration to the probability that a susceptible person becomes infected. Following Riley *et al.* (1978), the infection risk can be related to the concentration according to

$$P(t) = 1 - \exp\left[-I \int_0^t \eta C(\tau)\,\mathrm{d}\tau\right], \tag{2.2}$$

where I describes the infectivity of the disease and η is a breathing rate (see Table 1 for units and values).

In order to capture the spatiotemporal evolution of aerosol concentration and infection risk, Lau *et al.* (2022) generalised (2.1) to account for spatial effects: advection of aerosols around a recirculating AC flow, and diffusion due to turbulent eddies. This results in an advection–diffusion–reaction (ADR) equation governing the 2D concentration around the recirculating loop, $\mathscr{C}$. This is an areal concentration (in aerosols/m^2), with different units to the volumetric concentration C (in aerosols/m^3) introduced above. The production term

is modified so that an infected person is modelled as a point source at location (x_0, y_0), i.e. $R/V \to R\delta(x - x_0)\delta(y - y_0)$. As in (2.1), the removal terms are treated as global sinks.

The Lau *et al.* (2022) model was validated against two superspreader outbreaks: one in a courtroom in Switzerland (Vernez *et al.*, 2021), and one in a restaurant in Guangzhou, China (Lu, 2020; Li, 2021). In both cases, the results agreed well with real-world observations. For both scenarios, the transport of aerosols was dominated by a recirculating airflow generated by AC units that were ineffective at removing aerosols.

In this paper, we introduce a local treatment of ventilation in addition to the global sink used in both Wells–Riley models (2.1) and Lau *et al.* (2022). The modelling framework detailed below is a generalisation of the Lau *et al.* (2022) framework. The assumptions that recover the Lau *et al.* (2022) model are highlighted after the current model is described.

2.2. Spatiotemporal model with local ventilation

Consider a three-dimensional (3D) room of volume V, with dimensions L_x, L_y, L_z, as depicted in Figure 1(*a*) (values given in Table 1). Following Lau *et al.* (2022), we assume a recirculating flow produced by a single AC vent along the top corner and introduce the arclength coordinate ξ, which follows the recirculating loop. This assumption is consistent with the real-life case studies (Vernez *et al.*, 2021; Li, 2021) with which Lau *et al.* (2022) validated their model. Moreover, van Hooff *et al.* (2012) measure the flow generated by a similar AC configuration and observe a recirculating flow throughout the majority of the room. Additional flow features are also reported by van Hooff *et al.* (2012), such as a fast-moving jet near the ceiling and a counter-rotating loop near the top corner opposite the AC unit, both of which are confined to the top 15% of the room ($z > 2.55$ m here). These flow features are neglected from the current modelling framework since we assume that aerosols are produced at head height (≈ 1.5 m, half the height of the room), so these near-ceiling structures are assumed to have a negligible effect on aerosol transport.

The distance between the recirculation layers is taken to be $L_z/2$ and the total arclength is assumed to be $2L_x$ (as in Lau *et al.*, 2022). The height and arclength of the recirculating loop were determined by inspection of the recirculating flow reported by van Hooff *et al.* (2012).

The local ventilation system employed here is inspired by a common purifier design – a cylindrical device that draws air in through the top and expels air radially outwards near the bottom (Dbouk *et al.*, 2021). Inside the device, air passes through a filter which traps entrained particles. The filter efficacy ζ is the proportion of particles that are trapped by the filter, and hence removed from the room. We will assume that no aerosols that pass through the purifier re-enter the room, so $\zeta = 1$. This assumption is common in purifier modelling (Burgmann & Janoske, 2021; Dbouk *et al.*, 2021).

We will denote the radius of this device by r and assume that it extends over both recirculating layers: air is drawn into an inlet in the upper layer and expelled from an outlet in the lower layer.

Figure 1(*b*) shows the computational domain (ξ, y). The left/right halves correspond to the upper/lower layers and the purifier inlet and outlet appear as circles removed from the domain, with boundaries

$$\partial_{\text{in}} = \{(\xi, y) : |(\xi, y) - (x_p, y_p)| = r\}, \tag{2.3a}$$

$$\partial_{\text{out}} = \{(\xi, y) : |(\xi, y) - (2L_x - x_p, y_p)| = r\}, \tag{2.3b}$$

where (x_p, y_p) denotes the location of the centre of the purifier in the (x, y)-plane, and we will assume throughout this work that the purifier is in the centre of the room.

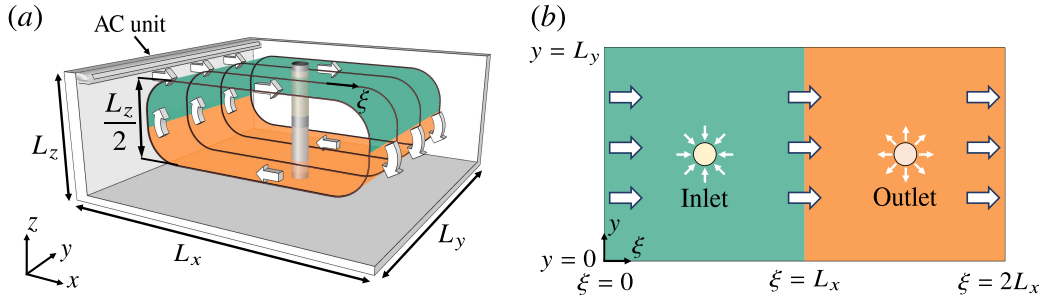

Figure 1: *A 3D room with dimensions L_x, L_y, L_z is shown in (a). A cylindrical local ventilation system crosses the two recirculating layers and the arclength coordinate ξ follows the recirculating loop. The computational domain (ξ, y) is shown in (b).*

In this quasi-3D model the device extends the entire height of the room, which is significantly taller than real-life purifiers. This simplification allows for a comparison with the model of Lau *et al.* (2022) while still offering useful and practical insights into the local effects of air purifiers.

Consider a single infectious individual at $\boldsymbol{x}_0 = (x_0, y_0)$ and talking continuously. Talking produces around 10 times as many aerosols as breathing (Asadi *et al.*, 2019): a reasonable worst-case scenario for an asymptomatic person. The infectious source will be placed in the top recirculating loop ($\xi = x_0$), meaning the infectious person is standing (e.g. a presenting teacher or lecturer). Let $\mathscr{C}(\xi, y, t)$ denote the concentration of aerosols (in aerosols/m^2) around the 2D recirculating loop depicted in Figure 1(*b*). We assume, as in Lau *et al.* (2022), that $\mathscr{C}(\xi, y, t)$ is governed by the ADR equation

$$\frac{\partial \mathscr{C}}{\partial t} + \nabla \cdot (\boldsymbol{v}\mathscr{C}) - \nabla \cdot (K \nabla \mathscr{C}) = R\delta(\xi - x_0)\delta(y - y_0) - (\lambda + \beta + \sigma)\mathscr{C}, \qquad (2.4)$$

where $\boldsymbol{v} = (u, v)$ is a vector field describing the airflow around the recirculating loop; K is the eddy diffusion coefficient; R is the (constant) aerosol production rate; and λ, β, σ are global removal rates due to ventilation, biological deactivation, and gravitational settling, respectively. Parameter values are given in Table 1; more details are provided in Lau *et al.* (2022).

Following Lau *et al.* (2022), we model the inbuilt ventilation with the global removal term λ and set $\lambda = 2 \times 10^{-4}$ s^{-1}; the 'poor ventilation' scenario of Lau *et al.* (2022) (from classroom data, Guo *et al.*, 2008). This reflects a broken or poorly maintained AC system that moves air around but is ineffective at removing aerosols (Lu, 2020) with an air exchange rate of 0.7 Air Changes per Hour (ACH). ACH will be given to 1 decimal place throughout this paper.

Gravitational settling is treated here as a global sink. It is assumed that aerosols land on the ground with a given rate σ and do not return to the air thereafter (i.e. they are removed from the room). Following Lau *et al.* (2022), the effect of gravity in transporting aerosols from the top layer of the recirculating loop to the bottom is neglected, since this process occurs over much longer time-scales than the transport of the aerosols along the recirculating loop.

Aerosol production begins at $t = 0$, so we set the initial condition $\mathscr{C}(\xi, y, 0) = 0$. Periodic conditions across the left and right boundaries ($\xi = 0, 2L_x$) complete the recirculating loop,

Table 1: *Parameters and their values.*

Parameter	Symbol	Value	Source
Room length	L_x	8 m	Lau *et al.* (2022)
Room width	L_y	8 m	Lau *et al.* (2022)
Room height	L_z	3 m	Lau *et al.* (2022)
Room volume	V	192 m^3	$L_x \times L_y \times L_z$
AC airflow speed	u_0	0.15 ms^{-1}	ASHRAE (2020)
Aerosol emission rate (talking)	R	5 aerosols/s	(Lau *et al.*, 2022)
Virus deactivation rate	β	1.7×10^{-4} s^{-1}	van Doremalen (2020)
Gravitational settling rate	σ	1.1×10^{-4} s^{-1}	De Oliveira *et al.* (2021)
Air exchange rate (rate of aerosol removal by ventilation)	λ	0.7 ACH: 2×10^{-4} s^{-1} 1.4 ACH: 4.0×10^{-4} s^{-1} 6 ACH: 1.7×10^{-3} s^{-1}	(Guo *et al.*, 2008) see Table 2 see Table 2
Turbulent eddy diffusion coefficient	K	0.7 ACH: 5.3×10^{-3} m^2s^{-1} 1.4 ACH: 1.0×10^{-2} m^2s^{-1} 6 ACH: 4.5×10^{-2} m^2s^{-1}	Foat *et al.* (2020), (2.7) Foat *et al.* (2020), (2.7) Foat *et al.* (2020), (2.7)
Breathing rate	η	1.3×10^{-4} m^3s^{-1}	Hallett *et al.* (2020)
Infectivity constant	I	0.0069	Lau *et al.* (2022)
Location of purifier centre	(x_p, y_p)	(4,4) m	Room centre: $(L_x, L_y)/2$
Radius of purifier	r	0.1 m	

$$\mathscr{C}(0, y, t) = \mathscr{C}(2L_x, y, t), \tag{2.5a}$$

$$\frac{\partial \mathscr{C}}{\partial \xi}(0, y, t) = \frac{\partial \mathscr{C}}{\partial \xi}(2L_x, y, t), \tag{2.5b}$$

and there is no flux through the walls at $y = 0, L_y$,

$$\frac{\partial \mathscr{C}}{\partial y}(\xi, 0, t) = \frac{\partial \mathscr{C}}{\partial y}(\xi, L_y, t) = 0. \tag{2.5c}$$

At the purifier inlet, we assume that aerosols are removed solely through advection (and cannot escape through diffusion). We therefore set zero diffusive flux here

$$\hat{\boldsymbol{n}} \cdot (K \nabla \mathscr{C}) = 0 \ \text{ on } \ \partial_{\text{in}}, \tag{2.6a}$$

which is also known as the Danckwerts condition (Danckwerts, 1953). The assumption that $\zeta = 1$ (the purifier filter traps all aerosols that pass through the device) means that no aerosols enter the domain through the purifier outlet. We thus set zero total (diffusive and advective) flux there,

$$\hat{\boldsymbol{n}} \cdot (\boldsymbol{v}\mathscr{C} - K \nabla \mathscr{C}) = 0 \ \text{ on } \ \partial_{\text{out}}. \tag{2.6b}$$

Here, $\hat{\boldsymbol{n}}$ denotes the unit vector normal to each boundary, directed out of the domain.

We extend the formula for the diffusion coefficient, K, from Foat *et al.* (2020). The turbulent eddies generated by the AC unit and purifier have different characteristic lengths

(due to different vent sizes) and different characteristic velocities, hence the turbulent dissipation associated with each will be different. Letting K_{ac} and K_p denote the turbulent diffusion coefficients associated with the AC unit and purifier (respectively), the formula from Foat *et al.* (2020) gives

$$K_{ac} = c\lambda\sqrt[3]{\frac{V^2}{2}}, \qquad K_p = c\lambda_p\sqrt[3]{\frac{V^2}{2}},$$

where λ_p is the air exchange rate of the purifier (discussed below) and we have assumed that there is a single vent of each size. Here, $c = c_v/\sqrt[3]{c_\varepsilon}$, where c_v is the von Karman constant and c_ε is the constant of proportionality in Taylor's dissipation law. Following the rationale of Bodin (1979) and Karlsson *et al.* (1994) we assume $c_\varepsilon = c_v^3$, giving $c = 1$ (as in Lau *et al.*, 2022).

The total eddy diffusion coefficient throughout the room is then assumed to be the sum of K_{ac} and K_p, giving

$$K = (\lambda + \lambda_p)\sqrt[3]{\frac{V^2}{2}}, \tag{2.7}$$

Several alternative combinations of K_{ac} and K_p were explored and found to produce similar results to those presented below. The expression (2.7) was chosen due to its mathematical simplicity and also because it produces the same value of K for equivalent global and local ventilation levels, making direct comparison straightforward. However, by assuming a constant K throughout the room, the model does not account for the increased levels of diffusion anticipated near to the purifier. The exact form that a spatially varying K would take has not been determined in the literature, to the best of our knowledge. To incorporate this feature into the model would necessitate a detailed study of turbulent eddy diffusion, which is outside the scope of this work.

Due to the inherent 3-dimensionality of turbulence, it is possible for turbulent eddies to transport aerosols between the upper and lower layers of the recirculating loop. This effect is neglected here under the assumption that these layers are sufficiently separated to evolve independently. This is a reasonable assumption for small K.

Following Lau *et al.* (2022), we assume that the majority of aerosols remain within the recirculating loop and consider the height-averaged concentration over the loop height $(L_z/2)$. This concentration, in aerosols/m^3, is given by

$$C(x, y, t) = \frac{\mathscr{C}(\xi = x, y, t) + \mathscr{C}(\xi = 2L_x - x, y, t)}{L_z/2}. \tag{2.8}$$

Here, we have divided the recirculating loop into an upper layer, $\xi \in [0, L_x]$ and a lower layer, $\xi \in [L_x, 2L_x]$, as depicted in Figure 1, to determine the height-averaged concentration, C. This represents the concentration of particles (in aerosols/m^3) at a given $(x, y) \in [0, L_x] \times [0, L_y]$ in the 3D room, whereas $\mathscr{C}$ represents the concentration (in aerosols/m^2) at a given $(\xi, y) \in [0, 2L_x] \times [0, L_y]$ on the 2D recirculating loop.

The Lau *et al.* (2022) model is a special case of the model described above, and is recovered by removing the purifier (and hence the internal boundaries ∂_{in} and ∂_{out}) and assuming a constant, unidirectional flow around the recirculating loop, $\boldsymbol{v} = (u_0, 0)$. All other modelling assumptions are the same.

2.3. Infection risk

The risk of infection to a susceptible person at any (x, y) is calculated using

$$P(x, y, t) = 1 - \exp\left[-I\int_0^t \eta C(x, y, \tau)\,\mathrm{d}\tau\right], \tag{2.9}$$

Table 2: *Parameters for two purifiers, with $\lambda = 2 \times 10^{-4}\ s^{-1}$ (0.7 ACH).*

Parameter	Symbol	Weak purifier	Strong purifier	Source
Clean Air Delivery Rate	CADR	140 m^3h^{-1}	1,000 m^3h^{-1}	*
Flow-rate	Q	0.039 m^3s^{-1}	0.28 m^3s^{-1}	CADR/3,600
Air velocity into purifier	v_p	0.04 ms^{-1}	0.3 ms^{-1}	(2.14)
Purifier air exchange rate	λ_p	2.0×10^{-4} s^{-1}	1.5×10^{-3} s^{-1}	Q/V
Purifier ACH		0.7 ACH	5.3 ACH	$3{,}600\lambda_p$
Total air exchange rate	λ_{tot}	4.0×10^{-4} s^{-1}	1.7×10^{-3} s^{-1}	$\lambda + \lambda_p$
Equivalent global ACH		1.4 ACH	6.0 ACH	$3{,}600\lambda_{\text{tot}}$

* Weak purifier: Dbouk *et al.* (2021), Strong purifier: Kähler *et al.* (2020).

where I is the infectivity constant of the virus and η is the breathing rate (see Table 1). This is a spatiotemporal version of (2.2), the infection risk used in Wells–Riley models, and the same as that used in the Lau *et al.* (2022) model.

2.4. Airflow

In Lau *et al.* (2022), aerosols are advected around the recirculating loop at constant speed u_0 (Table 1). Here, we assume that the recirculating loop remains coherent in the presence of a purifier, but we do not assume constant velocity. We assume that air enters and leaves the purifier with a specified constant speed v_p and this leads to a modified $\boldsymbol{v} = (u, v)$ such that

$$\boldsymbol{v} \cdot \hat{\boldsymbol{n}} = v_p \quad \text{on} \quad \partial_{\text{in}}, \tag{2.10a}$$

$$\boldsymbol{v} \cdot \hat{\boldsymbol{n}} = -v_p \quad \text{on} \quad \partial_{\text{out}}. \tag{2.10b}$$

We also require that $\boldsymbol{v}$ satisfies the periodic boundary condition,

$$\boldsymbol{v}(0, y) = \boldsymbol{v}(2L_x, y). \tag{2.11}$$

The velocity vector field that satisfies (2.10) and (2.11) is determined using the Shear Stress Transport (SST) turbulent flow solver (Menter, 1994) in COMSOL Multiphysics® (see COMSOL Inc., 2017). A turbulent flow solver is used since $Re > 10,000$ and hence numerical solutions to the Navier–Stokes equations were found to be sensitive to the mesh size. The resulting 2D flow in the (ξ, y)-plane does not incorporate the diffusive properties of a true 3D turbulent flow; the spreading of aerosols by small-scale turbulent eddies is accounted for by the eddy diffusion coefficient K, discussed above.

Imposing no-slip and no-penetration conditions at the walls,

$$\boldsymbol{v}(\xi, 0) = \boldsymbol{v}(\xi, L_y) = (0, 0), \tag{2.12}$$

and setting a suitable pressure gradient over the periodic boundaries to ensure

$$\max_y u(\xi = 0, y) = u_0, \tag{2.13}$$

we run the SST solver until a steady state is reached. This steady velocity, $\boldsymbol{v}$, is then used in the ADR equation (2.4). The results are compared against those of Lau *et al.* (2022) for: (i) no purifier, and (ii) a switched-off purifier ($v_p = 0$). There is good agreement in both cases provided (2.13) is satisfied. Several turbulent models were compared and all resulted

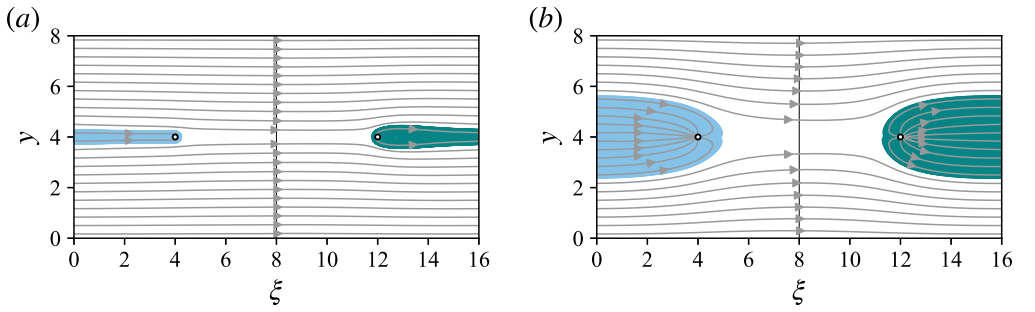

Figure 2: *The airflow streamlines in the (ξ, y)-plane are shown for (a) the weak purifier ($v_p = 0.04$) and (b) the strong purifier ($v_p = 0.3$). The shaded regions indicate streamlines that pass through the purifier inlet (left) and the purifier outlet (right).*

in a similar concentration distribution $\mathscr{C}$. The details of the SST flow solver used here are provided in Appendix A.

The steady-state assumption is consistent with van Hooff *et al.* (2012) and realistic for many locations (e.g. classrooms and offices) where the air conditioning is managed automatically and is therefore expected to have settled into a steady state prior to use. Note that during the development of this steady recirculating flow, we would anticipate complex transient effects such as multiple vortices of different sizes.

Two purifier settings are considered based on the Clean Air Delivery Rate (CADR) of purifiers used in experimental and computational studies. We define a *weak purifier* with a CADR of 140 $\mathrm{m^3h^{-1}}$, representative of devices for small spaces such as domestic rooms (Dbouk *et al.*, 2021) and individual offices; and a *strong purifier* with a CADR of 1,000 $\mathrm{m^3h^{-1}}$, representative of devices for larger spaces such as classrooms (Kähler *et al.*, 2020) and open-plan offices.

Let Q denote the flow-rate through the device in $\mathrm{m^3s^{-1}}$. In general, the CADR (stated in $\mathrm{m^3h^{-1}}$ by convention) is given by ζQ (for filter efficacy ζ). Here, the assumption $\zeta = 1$ means the CADR and flow-rate Q are equivalent. For a cylindrical purifier (circumference $2\pi r$) with an inlet half the height of the room ($L_z/2$),

$$Q = \pi r L_z v_p. \tag{2.14}$$

Using $v_p = Q/\pi r L_z$ (see Table 2) as the air speed at the inlet and outlet boundaries in (2.10), we use the SST solver to determine the velocity field $\boldsymbol{v}$ for each purifier.

Each purifier is compared with an equivalent increase in the global removal term λ. The air exchange rate associated with each purifier is given by $\lambda_p = Q/V$, which we add to the global removal rate of the AC unit (0.7 ACH) to determine a total air exchange rate, $\lambda_{\mathrm{tot}} = \lambda + \lambda_p$ (see Table 2). The weak purifier doubles the total air exchange to 1.4 ACH, less than half the recommended ventilation for classrooms – 3 ACH for 30 occupants (ASHRAE, 2022). The total air exchange rate with the strong purifier is 6 ACH, exceeding this recommendation and also sufficient to meet the guidelines for times of heightened infection risk, provided the number of occupants is halved (ASHRAE, 2023).

The streamlines of the airflow $\boldsymbol{v}$ are shown in Figure 2 for both purifiers. The flow is broadly unidirectional for the weak purifier (Figure 2*a*). Regions in which the streamlines are directed into or out of the purifier are shaded and take up a greater area for the strong purifier (Figure 2*b*). In both cases, these regions meet at the periodic boundary.

2.5. Terminology: global and local ventilation models

To improve clarity in the discussions below, we here define shorthand labels that refer to the models explored. There are three features that all models compared have in common: (i) the computational domain, which is depicted in Figure 1(*b*); (ii) the SST solver is used to determine the airflow $\boldsymbol{v}$; and (iii) the global ventilation rate λ is non-zero.

The term *global ventilation model* here refers to cases in which there are no local ventilation effects. To ensure the computational domain is consistent, the purifier is present but switched off, $v_p = 0$. This global ventilation model is subtly different to the model of Lau *et al.* (2022) due to the existence of the boundaries ∂_{in}, ∂_{out} and the non-uniform vector field $\boldsymbol{v}$. Aside from these minor differences, the underlying modelling assumptions are the same. This model was compared with results reported in Lau *et al.* (2022) and the contours of aerosol concentration C were found to be virtually indistinguishable except in small regions near to the switched-off purifier where differences remained minimal.

We consider three global ventilation levels, which will be referred to by the ACH: The control case 0.7 ACH, in which the only ventilation is provided by the ineffective AC unit; 1.4 ACH, equivalent to the total air exchange rate for the weak purifier; and 6 ACH, equivalent to the total air exchange rate for the strong purifier.

The term *local ventilation model* refers to the cases in which the purifier is switched on, i.e. $v_p \neq 0$. In these cases, the global ventilation rate is that of the control case, 0.7 ACH, so we are considering the combined ventilation of the ineffective AC unit (treated globally) and the purifier (treated locally). The two local ventilation cases explored are referred to by the purifier strength: The weak purifier (CADR of 140 m^3h^{-1}); and the strong purifier (CADR of 1,000 m^3h^{-1}).

2.6. Computational speed

The model was solved in COMSOL Multiphysics® on a triangular mesh using the predefined 'Finer' mesh, with a maximum element size of 0.224 m. The automatic 'Fluid dynamics' calibration resolved the boundary layers with smaller elements near to boundaries. The point source was approximated by uniform production within a small circle, radius $r_s = 2.5$ mm. Consequently, a finer mesh was produced around $\boldsymbol{x}_0 = (x_0, y_0)$. To ensure the symmetry of the problem was numerically realisable, a symmetric mesh about the centreline $y_0 = L_y/2$ was used. For scenarios in which $y_0 \neq L_y/2$ this resulted in an additional region of finer meshing near $(x_0, L_y - y_0)$, resulting in slightly more mesh elements than when $y_0 = L_y/2$. Each mesh contained approximately $21,000$ nodes (though the precise number differed for each $\boldsymbol{x}_0$). Both the flow field and the ADR equation were solved on the same mesh.

The mesh independency was explored as follows: all parameters were fixed and the problem (both airflow and ADR equation) was solved using the automatic resolution settings ranging from 'Coarser' to 'Extremely Fine'. For direct comparison, each solution was interpolated onto a fine uniform grid (using cubic splines), and the relative error between the 'Extremely Fine' mesh (around 90,000 nodes) and each of the other meshes was calculated at each grid point, then integrated over the domain (using Simpson's rule). The 'Finer' mesh ensured a discrepancy of the order of 10^{-3} and resulted in plots that were visually indistinguishable from those for the 'Extremely Fine' mesh.

Simulations were performed on a Lenovo IdeaPad Flex 5 laptop, with a 1.3 GHz 4-core Intel Core i7-1065G7 processor and 8 GB of RAM. For each airflow simulation (switched-off purifier, weak purifier, strong purifier) to reach a steady state, computation takes approximately 10 minutes. For the ADR equation (2.4), an event lasting 4 hours takes around 5 minutes to run, including calculation of the infection risk (2.9). At these computational speeds, advice and guidance can be quickly updated with new information

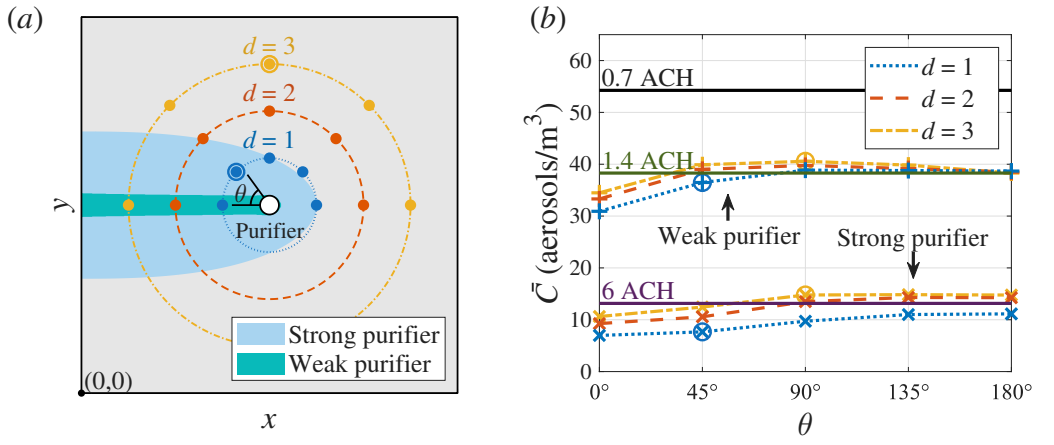

Figure 3: *In (a), the infectious source locations, $\boldsymbol{x}_0$, are depicted by filled circles and the regions where all streamlines are directed into the purifier inlet (Figure 2) are shaded for each purifier. In (b), the average aerosol concentration, $\bar{C}$, after 4 hours is shown for the weak (+) and the strong (×) purifiers for these $\boldsymbol{x}_0$. The global ventilation cases are also shown in (b), depicted as horizontal lines (labelled with the ACH). The cases explored further in Figures 4 and 5 are indicated with circles.*

during a fast-changing epidemic.

3. Average aerosol concentration

We define the average aerosol concentration in the room as

$$\bar{C}(t) = \frac{1}{V}\iint_{\Omega} \mathscr{C}(\xi, y, t)\,\mathrm{d}\xi\,\mathrm{d}y, \tag{3.1}$$

where Ω denotes the computational domain depicted in Figure 1(*b*). Taking appropriate integrals of (2.4), the divergence theorem is applied to the advective and diffusive terms, giving

$$\frac{\partial \bar{C}}{\partial t} = \frac{R}{V} - (\lambda + \beta + \sigma)\bar{C} - \frac{1}{V}\oint_{\partial_{\mathrm{in}}} v_p \mathscr{C}\,\mathrm{d}l, \tag{3.2}$$

where l denotes a line element on ∂_{in}. When $v_p \neq 0$, the boundary integral (describing aerosol removal by the purifier) depends on the values of $\mathscr{C}$ on the purifier inlet boundary ∂_{in} (2.3), which depend on the distribution of aerosols around the room. Hence, $\bar{C}$ implicitly depends on the location of the infectious source $\boldsymbol{x}_0$ and strength of the purifier. When $v_p = 0$ there is no local ventilation (as in Lau *et al.*, 2022), the boundary integral vanishes, and (3.2) is equivalent to the Wells–Riley model (2.1). In this case the solution to (3.2) is given by

$$\bar{C}(t) = C^*\left[1 - \mathrm{e}^{-(\lambda+\beta+\sigma)t}\right], \quad \text{where} \quad C^* = \frac{R}{(\lambda + \beta + \sigma)V}. \tag{3.3}$$

Hence, $\bar{C}$ does not depend on $\boldsymbol{x}_0$ or $\boldsymbol{v}$ for the global ventilation cases, and $\bar{C} \to C^*$ as $t \to \infty$.

We express the location of the infectious source relative to the purifier location as

$$\boldsymbol{x}_0 = (x_0, y_0) = (x_p - d\cos\theta, y_p + d\sin\theta), \tag{3.4}$$

where d is the distance from the purifier and θ is the angle (in degrees) from the line $y = L_y/2$. The problem is symmetric in this line so we consider only $\theta \in [0°, 180°]$. In Figure 3(a), we show all choices of (d, θ) considered here.

To compare the long-time behaviour of the different ventilation models, $\bar{C}$ is plotted in Figure 3(b) after an event of 4 hours. This duration is representative of certain social settings (e.g. restaurants), activities within all-day events (such as conferences, workshops and networking events), and time spent working in open-plan offices. For all the cases considered here, $\mathscr{C}$ reaches a steady state within this time.

For the global ventilation models, $\bar{C} = C^*$ (3.3), which we evaluate for 0.7 ACH, 1.4 ACH, and 6 ACH; plotted as horizontal lines in Figure 3(b). There is good agreement between each purifier and the equivalent global ventilation for most (d, θ) choices. For the weak purifier, the only significant deviation is when $\theta = 0$ (for all values of d). For the strong purifier, the discrepancy is significant for $d = 1$ (for all values of θ) and for small θ when $d = 2, 3$. Where the results differ the most, the global ventilation overestimates $\bar{C}$ compared to the local purifier model. When $d = 2, 3$, the global ventilation model underestimates $\bar{C}$ for some θ, but the discrepancy is relatively small.

In Figure 3(b), we show that $\bar{C}$ increases with d for both purifiers; purifiers are less effective when the infectious person is further away. This aligns with the intuitive expectation that placing the infectious source nearer to the purifier would allow the purifier to capture a greater number of aerosols, hence reducing the average concentration, $\bar{C}$. Also, both purifiers are more effective (with $\bar{C}$ decreasing) when the infectious person is located in the shaded region where all streamlines enter the purifier inlet. In these cases, the global ventilation overestimates the concentration. When $\boldsymbol{x}_0$ is outside of these regions, there is less variation in $\bar{C}$ and closer agreement between the ventilation models.

4. Spatial distribution of aerosols

The spatiotemporal model also provides information on the spatial distribution of aerosols around the room. The local and global ventilation models were compared for the infectious source locations depicted in Figure 3(a). Contour plots showing the spatial variation of C after 4 hours (as in Figure 3) are given in Figures 4 and 5 for some representative examples. For this discussion, we will denote the concentration for the local ventilation model (purifier) by C_p and for the equivalent global ventilation model by C_g.

The concentration around the room is shown in Figure 4 when $(d, \theta) = (1, 45°)$ for both purifiers and the equivalent global ventilations. In Figures 4(a,b), C_p and C_g are shown (respectively) for the weak purifier. There is a similar concentration throughout the room for both ventilation models but $C_p < C_g$ everywhere. The largest discrepancies are: below and to the left of the purifier; and to the right of the infectious source. Similar features were observed for all cases in which the infectious source is located near to (but outside of) the region where streamlines are directed into the purifier inlet (Figure 3a).

Figures 4(c,d) show C_p, C_g (respectively) for the strong purifier. In this case, the global ventilation model significantly overestimates the concentration compared to the local ventilation model. For instance, $C_g > 21$ aerosols/m^3 everywhere in Figure 4(d) whereas $C_p < 21$ aerosols/m^3 in the majority of the room in Figure 4(c). These observations are indicative of all cases where the infectious source lies inside the region where streamlines are directed into the purifier inlet (see Figure 3a).

In Figure 5, we consider the distribution of aerosols when $(d, \theta) = (3, 90°)$. These are representative examples for the cases where the infectious source is far away from the region where the streamlines are directed into the purifier inlet.

Comparing C_p and C_g for the weak purifier (Figures 5a,b), the concentration is similar

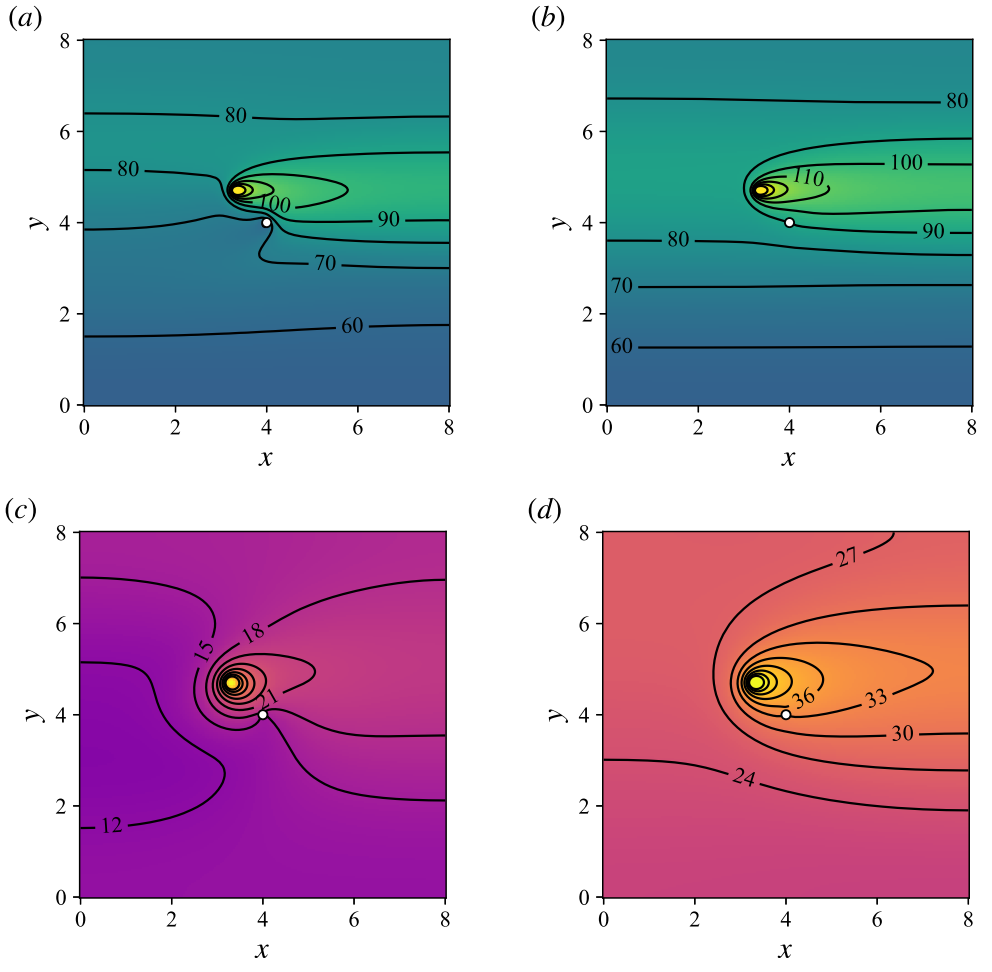

Figure 4: *Contour plots of the aerosol concentration C after 4 hours for an infectious source at* $\boldsymbol{x}_0$ (3.4) *with* $(d, \theta) = (1, 45°)$ *(see Figure 3a). The concentration is shown for (a) the weak purifier* (C_p) *and (b) the equivalent global ventilation of 1.4 ACH* (C_g)*, both with contours at intervals of 10 aerosols/m*^{3}*. The concentration is shown for (c) the strong purifier* (C_p) *and (d) the equivalent global ventilation of 6 ACH* (C_g)*, both with contours at intervals of 3 aerosols/m*^{3}*.*

throughout the room, except for the region $y > 5$, where C_p is approximately one contour level (14 aerosols/m^3) larger than C_g. There are regions in the room where $C_p < C_g$ (near the purifier) and where $C_p > C_g$ (near the infectious source), with the dashed red line (the same in both plots) showing the boundary between these regions, i.e. where $C_p = C_g$ (no such lines appear in Figure 4 since $C_p < C_g$ everywhere in those cases).

For the strong purifier example shown in Figures 5(*c,d*), the spatial distribution of aerosols differs more significantly between the ventilation models. The region where $C_p < C_g$ is larger in this case, but where $C_p > C_g$ the concentration difference ranges from around 1 contour level (5 aerosols/m^3), in the top left and bottom right of the room, to around 2 contour levels, in the top right (near to the infectious source). This suggests that the global ventilation model better captures the aerosol distribution of the weak purifier than

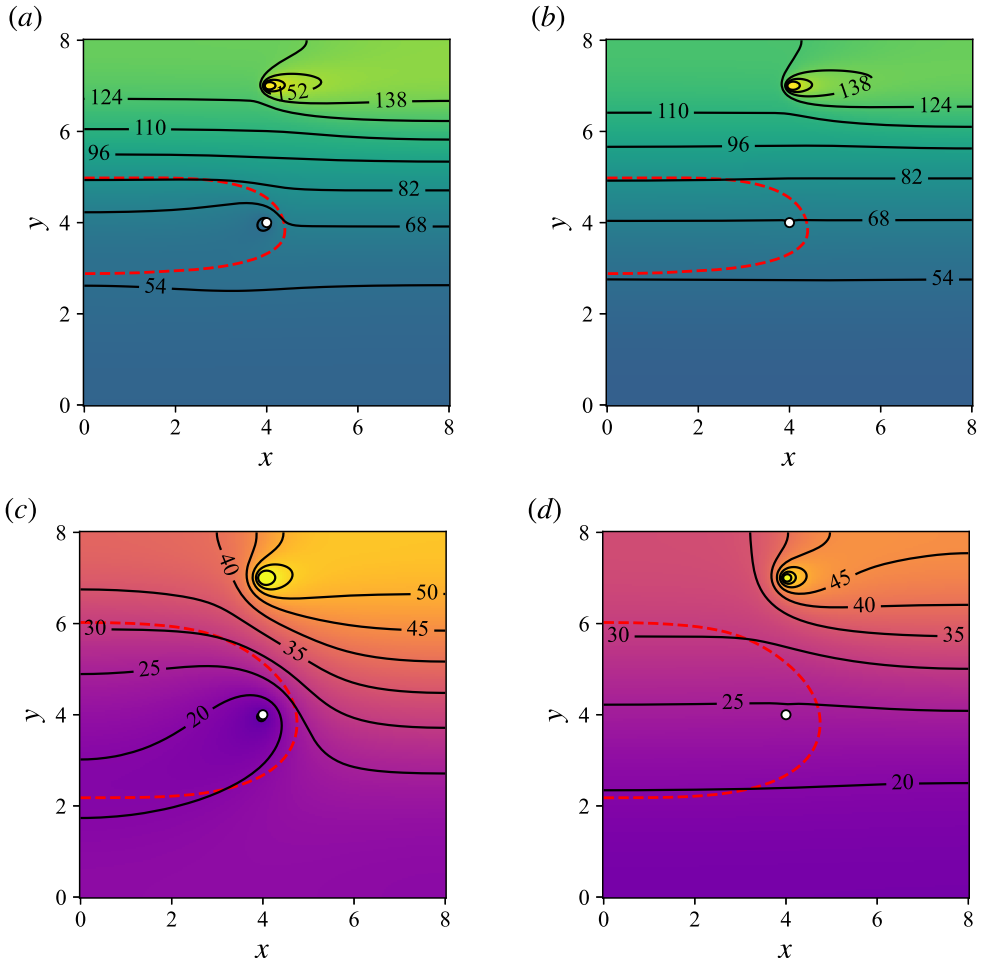

Figure 5: *Contour plots of the aerosol concentration C after 4 hours for an infectious source at* $\boldsymbol{x}_0$ (3.4) *with* $(d, \theta) = (3, 90°)$ *(see Figure 3a). The concentration is shown for (a) the weak purifier* (C_p) *and (b) the equivalent global ventilation of 1.4 ACH* (C_g)*, both with contours at intervals of 14 aerosols/m*^{3}*. The concentration is shown for (c) the strong purifier* (C_p) *and (d) the equivalent global ventilation of 6 ACH* (C_g)*, both with contours at intervals of 5 aerosols/m*^{3}*. Additional dashed lines show where* $C_p = C_g$.

the strong purifier.

5. Infection risk to susceptible people

Our spatially varying model allows us to determine the infection risk to susceptible people at specific locations, (2.9). We express the location of a susceptible person $\boldsymbol{x}_s$ as

$$\boldsymbol{x}_s = (x_s, y_s) = (x_p - d_s \cos(\theta + \phi), y_p + d_s \sin(\theta + \phi)), \tag{5.1}$$

where ϕ is the angle between $\boldsymbol{x}_0$ and $\boldsymbol{x}_s$, and d_s is the distance from the purifier.

To reflect a scenario in which the susceptible and infectious individuals are in close proximity, we consider $d = d_s = 1$ (note that $d = 1$ is the case with the greatest discrepancy

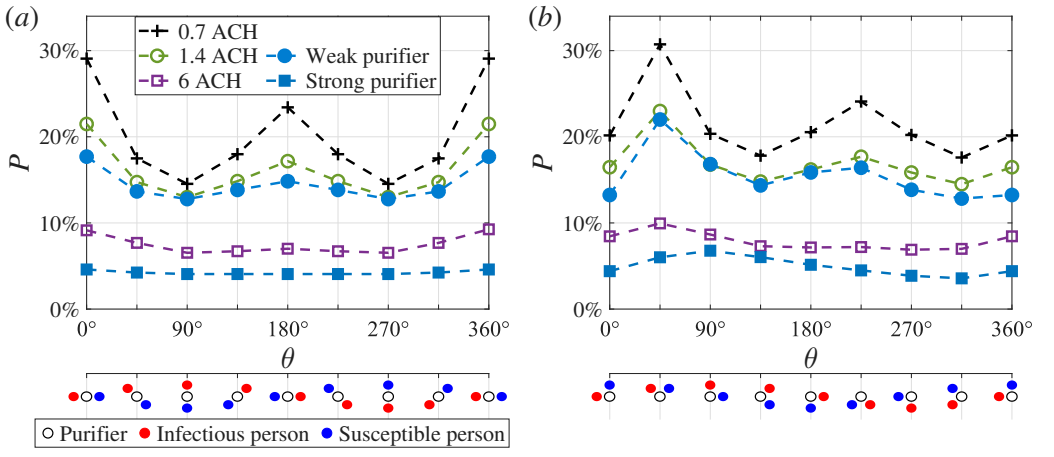

Figure 6: *The infection risk, P (equation* (2.9)*), to the susceptible person at* $\boldsymbol{x}_s$ *(see* (5.1)*) after 1 hour with (a)* $\phi = 180°$ *and (b)* $\phi = 90°$*. Global ventilation cases are labelled with their ACH value (open symbols) and the equivalent local ventilation (purifier) is depicted by filled symbols of the same shape. Schematics in the lower axes show the locations of the infectious and susceptible people for each* θ*.*

between the local and global ventilation models in Figure 3). This is reflective of classrooms, lectures, and meetings, with 1 hour being a representative event duration. However, in reality, the strong purifier is potentially too large and noisy for use in such a setting.

Two configurations of the susceptible and infectious people are considered: (i) they are opposite each other with the purifier in between them, $\phi = 180°$ (Figure 6*a*); and (ii) they are to one side of the purifier, $\phi = 90°$ (Figure 6*b*). Figure 6 shows the infection risk to the susceptible person after 1 hour, with the scenario for each θ depicted on the lower axes. In Figure 6(*a*), P is symmetric around $\theta = 180°$ because both the ADR equation and the airflow are symmetric in the line $y = L_y/2$. Moreover, the case $\phi = -90°$ can be deduced from Figure 6(*b*) by reflection in this line ($\theta \to 360° - \theta$).

After 1 hour, the infection risk is below 40% in all cases and the global ventilation model overestimates the infection risk. The weak purifier has had only a marginal effect when compared against the baseline example of 0.7 ACH, and shows close agreement with the corresponding global ventilation of 1.4 ACH. The infection risk is lower for the strong purifier than for the equivalent global ventilation of 6 ACH for all values of θ. The greatest discrepancy is when $\theta = 0°$, with the strong purifier predicting half the infection risk of the 6 ACH global ventilation (Figures 6*a,b*).

The streamlines of $\boldsymbol{v}$ again provide insight into these results. For the global ventilation models and the weak purifier, peaks occur when $y_0 = y_s$ due to the broadly unidirectional flow around the recirculating loop, with lower peaks when the aerosols travel further (e.g. $\theta = 180°$ in Figure 6*a*). For the strong purifier, the largest infection risk ($\theta = 90°$ in Figure 6*b*) corresponds to the susceptible person being directly downstream from the infectious person according to the significantly modified streamlines in this case (Figure 2*b*).

Under the well-mixed-room assumption, the infection risk is calculated based on the average aerosol concentration, $\bar{C}$ (3.3). This approach predicts the following infection risks: 8.8% for 0.7 ACH, 7.5% for 1.4 ACH, and 3.6% for 6 ACH. This is a significant underestimate compared to the corresponding values in Figure 6 since the proximity to the infectious source results in a concentration significantly greater than the room average at all times.

6. Summary and conclusions

Motivated by air purifiers, the spatiotemporal modelling framework of Lau *et al.* (2022) for airborne disease transmission was modified to incorporate local ventilation effects. For a weak purifier (CADR = 140 m^3h^{-1}) and a strong purifier (CADR = 1,000 m^3h^{-1}), the local ventilation model introduced here was compared against a global ventilation model (consistent with Lau *et al.*, 2022), with 1.4 ACH and 6 ACH, respectively.

For each purifier, the average aerosol concentration $\bar{C}$, after reaching a steady state, was compared for the local and global ventilation models, with good agreement in most cases (Figure 3). For the local ventilation model, $\bar{C}$ depends on the infectious source location and increasing the distance between the infectious person and the purifier increases the average concentration. The lowest values of $\bar{C}$ were observed when the infectious source is inside the regions where the airflow streamlines are directed into the purifier inlet (Figure 2). When the infectious source is inside these regions, the global ventilation model significantly overestimates $\bar{C}$. When the infectious source is located outside of these regions, there is better agreement between the two ventilation models, particularly for the weak purifier.

When the infectious person is located inside or near to these regions, the global ventilation model overestimates the aerosol concentration everywhere in the room (Figure 4). However, when the infectious source is far from the purifier, there are some regions where the global ventilation model predicts larger concentrations, and other regions where it predicts lower concentrations than the local ventilation model (Figure 5). In these cases, the agreement between the local and global ventilation models is better for the weak purifier.

The infection risk to susceptible people near the purifier after one hour was also considered (Figure 6). The weak purifier showed good agreement with the global ventilation model, whereas the strong purifier predicts a lower infection risk than the equivalent global ventilation (Figure 6). The largest discrepancies between the local and global ventilation models were observed when the susceptible person was located directly downstream from the infectious person according to the modified airflow streamlines (Figure 2). The global ventilation model overestimates infection risk compared to the local ventilation model in these cases.

When modelling airborne transmission, Wells–Riley models (e.g. Miller, 2021) offer very high computational speeds but are very simple, whereas CFD models, particularly those that track individual particles (e.g. Dbouk *et al.*, 2021), provide significant detail at much greater computational cost. The modelling framework of Lau *et al.* (2022) offers a compromise between these models, including spatial variation at low computational cost. Here, we increased the complexity by developing a model incorporating local ventilation over hours, the time frame over which airborne transmission occurs, while still retaining relatively small computational times; around five minutes of simulation time for 4-hour events.

In future, these fast simulations could allow a more thorough investigation, exploring factors such as purifier location, size, and strength. The model could be further developed by incorporating a spatially varying eddy diffusion coefficient or the unsteady airflow produced when the purifier is switched on at a given time. The local ventilation effects of air-conditioning, windows, doors, and other purifier designs could also be explored, with the caveat that such features may promote interaction between the recirculation layers, and hence undermine this underlying assumption. Experimental studies and CFD would provide insight into when the recirculating flow assumption is valid. Even in cases where this assumption breaks down, the rationale of using a simplified airflow to produce fast predictions could still be applied to explore different AC unit designs, different purifier designs, and other types of ventilation, provided an appropriate simplified airflow can be

determined.

Acknowledgements: The authors wish to acknowledge the contributions of Dr. Aaron English, Dr. Raquel González Fariña and Dr. Attila Kovács. We are grateful to Siân Grant for generating Figure 1(*a*).

Funding: A.P. and K.K. gratefully acknowledge funding from a Sêr Cymru 'Tackling COVID-19' grant, awarded by the Welsh Government. I.M.G. is grateful to the Royal Society for funding through a University Research Fellowship.

Declaration of interests: The authors report no conflict of interest.

A. Turbulent flow solver

A.1. Reynolds-averaged Navier–Stokes equations

Consider the Navier–Stokes equations

$$\rho\frac{\partial \boldsymbol{u}}{\partial t} + \rho(\boldsymbol{u}\cdot\nabla)\boldsymbol{u} = -\nabla p + \nabla\cdot\mu(\nabla\boldsymbol{u} + (\nabla\boldsymbol{u})^T), \tag{A 1a}$$

$$\nabla\cdot\boldsymbol{u} = 0, \tag{A 1b}$$

where $\boldsymbol{u} = (u_x, u_y)$ is the velocity field, p is the pressure, ρ is the fluid density and μ is the dynamic viscosity. The viscous terms are written in this form as it later highlights the viscosity-like effect of turbulent fluctuations on the flow, but for an incompressible flow with constant viscosity (such as air), $\nabla\cdot\mu(\nabla\boldsymbol{u} + (\nabla\boldsymbol{u})^T) = \mu\nabla^2\boldsymbol{u}$. We consider a 2D velocity field $\boldsymbol{u}$ for the current problem, but generally present equations in vector notation so that the derivation is applicable to 3D flows.

A Reynolds decomposition is applied to the flow variables,

$$\psi = \bar{\psi} + \psi', \tag{A 2}$$

where $\bar{\psi}$ is a time-averaged mean quantity, and ψ' represents turbulent fluctuations. This decomposition is applied for all flow variables, i.e. $\psi = u_x, u_y, p$. For consistency of notation with §2, we will refer to the time-averaged vector field $\bar{\boldsymbol{u}}$ as $\boldsymbol{v}$. Applying the decomposition (A 2) to (A 1) and time-averaging the resulting equations (noting that the time-average of fluctuation variables is zero) gives the Reynolds-averaged Navier–Stokes equations (RANS) governing the mean flow

$$\rho\frac{\partial \boldsymbol{v}}{\partial t} + \rho(\boldsymbol{v}\cdot\nabla)\boldsymbol{v} + \rho\overline{(\boldsymbol{u'}\cdot\nabla)\boldsymbol{u'}} = -\nabla\bar{p} + \nabla\cdot\mu(\nabla\boldsymbol{v} + (\nabla\boldsymbol{v})^T),$$

$$\nabla\cdot\boldsymbol{v} = 0,$$

where all the fluctuation terms vanish due to the time-averaging, except for the one remaining non-linear term. This term can be rewritten in terms of the Reynolds stress $\mathcal{R} = \rho\overline{(\boldsymbol{u'}\otimes\boldsymbol{u'})}$:

$$\rho\overline{(\boldsymbol{u'}\cdot\nabla)\boldsymbol{u'}} = \nabla\cdot\mathcal{R},$$

where the divergence operator is applied row-wise to the tensor $\mathcal{R}$. Note that this equivalence holds only for incompressible flows since in general we have $\nabla\cdot(\boldsymbol{a}\otimes\boldsymbol{a}) = (\boldsymbol{a}\cdot\nabla)\boldsymbol{a} + \boldsymbol{a}\cdot(\nabla\cdot\boldsymbol{a})$ for any vector field $\boldsymbol{a}$.

The term $\nabla \cdot \mathcal{R}$ represents the stress-like effect that turbulent fluctuations have on the mean flow. Following the Boussinesq approach, we assume that turbulence is of a purely diffusive nature, in which case the Reynolds stress can be written as

$$\mathcal{R} = \frac{2}{3}\rho k - \mu_T(\nabla \boldsymbol{v} + (\nabla \boldsymbol{v})^T),$$

where $k = \frac{1}{2}(u_x^2 + u_y^2)$ is the turbulent kinetic energy and μ_T is the eddy viscosity (or turbulent viscosity) of the flow. Both of these quantities are, in general, spatially dependent.

We hence write the RANS equations in the form

$$\rho\frac{\partial \boldsymbol{v}}{\partial t} + \rho(\boldsymbol{v}\cdot\nabla)\boldsymbol{v} + \frac{2}{3}\rho\nabla\cdot k = -\nabla\bar{p} + \nabla\cdot(\mu+\mu_T)(\nabla\boldsymbol{v} + (\nabla\boldsymbol{v})^T), \tag{A 4a}$$

$$\nabla\cdot\boldsymbol{v} = 0. \tag{A 4b}$$

Observe that μ_T appears alongside the viscosity μ, highlighting its interpretation as an additional viscous effect that arises from the small-scale turbulent fluctuations.

The system of differential equations (A 4) is solved subject to the boundary conditions (2.10), (2.11), and (2.12). However, in order to close the system, we require equations that govern the evolution of k and μ_T.

A.2. Shear Stress Transport (SST) turbulence model

The Shear Stress Transport (SST) turbulent flow model was developed by Menter (1994) to address the failure of pre-existing two-equation turbulence models (the k-ω and k-ε models) to predict the onset and amount of flow separation in adverse pressure gradient flows. The SST model interpolates between the k-ω model in the near-wall region, since this is a numerically robust method, and the k-ε model in the outer part of the boundary layer, where the k-ω model is highly sensitive to arbitrary freestream parameters. The version of the SST solver implemented in COMSOL includes some modifications to the original formulation (COMSOL Inc., 2017).

The model equations are formulated in terms of k, the turbulent kinetic energy, and ω, the dissipation per unit kinetic energy. The transport of these quantities is governed by

$$\rho\frac{\partial k}{\partial t} + \rho\boldsymbol{v}\cdot\nabla k = \mathcal{P} - \rho\alpha_0^* k\omega + \nabla\cdot\left[(\mu+\nu_k\mu_T)\nabla k\right], \tag{A 5a}$$

$$\rho\frac{\partial \omega}{\partial t} + \rho\boldsymbol{v}\cdot\nabla\omega = \frac{\rho\gamma}{\mu_T}\mathcal{P} - \rho\alpha\omega^2 + \nabla\cdot\left[(\mu+\nu_\omega\mu_T)\nabla\omega\right] + 2(1-f_{v1})\frac{\rho\nu_{\omega 2}}{\omega}\nabla\omega\cdot\nabla k, \tag{A 5b}$$

where the kinetic energy production term $\mathcal{P}$ is given by

$$\mathcal{P} = \min\left(\mu_T\left[\nabla\boldsymbol{v} : (\nabla\boldsymbol{v} + (\nabla\boldsymbol{v})^T) - \frac{2}{3}(\nabla\cdot\boldsymbol{v})^2\right] - \frac{2}{3}\rho k\nabla\cdot\boldsymbol{v}, 10\rho\alpha_0^* k\omega\right),$$

with : denoting the tensor scalar product.

Each of the model constants $\psi = \alpha, \gamma, \nu_k, \nu_\omega$ are interpolated between values appropriate for the inner, or near-wall, region denoted ψ_1 (equivalent to the k-ω model) and those appropriate for the outer region, away from the wall, denoted ψ_2 (equivalent to a transformed k-ε model), i.e.

$$\psi = f_{v1}\psi_1 + (1-f_{v1})\psi_2,$$

according to the interpolation function

$$f_{v1} = \tanh(\theta_1^2), \qquad \theta_1^2 = \min\left[\max\left(\frac{\sqrt{k}}{\alpha_0^* \omega l_w}, \frac{500\mu}{\rho\omega l_w^2}\right), \frac{4\rho\nu_{\omega 2}k}{CD_{k\omega} l_w^2}\right],$$
$$CD_{k\omega} = \max\left(\frac{2\rho\nu_{\omega 2}}{\omega}\nabla\omega\cdot\nabla k, 10^{-10}\right),$$

where l_w is the distance to the nearest wall (a quantity that is solved for on every mesh point prior to the running of the turbulent model).

The turbulence transport equations (A 5) can then be solved, with boundary conditions that come from setting $k = 0$ at the walls (since $\boldsymbol{v}$ vanishes here to satisfy no-slip) and

$$\lim_{l_w\to 0}\omega = \frac{6\mu}{\rho\alpha_1 l_w^2}.$$

To avoid the singularity at $l_w = 0$, we prescribe $\omega = \omega_w$ in the cells adjacent to the solid wall. Initial conditions for (A 5) are

$$k(t=0) = \left(\frac{\mu}{\rho(0.1 l_{\text{ref}})}\right)^2, \qquad \omega(t=0) = \frac{\sqrt{k(t=0)}}{0.1 l_{\text{ref}}},$$

where l_{ref} is a variable that feeds into the wall distance model.

The turbulent viscosity can be defined as

$$\mu_T = \frac{\rho b_1 k}{\max(b_1\omega, S f_{v2})},$$

where S is a characteristic magnitude of the velocity gradients, i.e. $S = \sqrt{2S_{ij}S_{ij}}$, where S_{ij} is the mean strain-rate tensor. The interpolation function f_{v2} is defined as

$$f_{v2} = \tanh(\theta_2^2), \qquad \theta_2 = \max\left(\frac{2\sqrt{k}}{\alpha_0^*\omega l_w}, \frac{500\mu}{\rho\omega l_w^2}\right).$$

The model parameters used here are the COMSOL default values (COMSOL Inc., 2017), but different notation is used here for consistency with the rest of the paper,

$$\begin{gathered}\alpha_1 = 0.75, \quad \gamma_1 = 5/9, \quad \nu_{k1} = 0.85, \quad \nu_{\omega 1} = 0.5,\\ \alpha_2 = 0.0828, \quad \gamma_1 = 0.44, \quad \nu_{k2} = 1, \quad \nu_{\omega 2} = 0.856,\\ \alpha_0^* = 0.09, \quad b_1 = 0.31.\end{gathered}$$

References

Asadi, S., Wexler, A. S., Cappa, C. D., Barreda, S., Bouvier, N. M. & Ristenpart, W. D. 2019 Aerosol emission and superemission during human speech increase with voice loudness. *Sci. Rep.* **9** (1), 1–10.

ASHRAE 2020 Standard 55-2020, Thermal environmental conditions for human occupancy.

ASHRAE 2022 Standard 62.1-2022, Ventilation and acceptable indoor air quality.

ASHRAE 2023 Standard 241-2023, Control of infectious aerosols.

Bodin, S. 1979 A predictive numerical model of the atmospheric boundary layer based on the turbulent energy equation. PhD thesis, Stockholm University.

Buonanno, G., Stabile, L. & Morawska, L. 2020 Estimation of airborne viral emission: Quanta emission rate of SARS-CoV-2 for infection risk assessment. *Environ. Int.* **141**, 105794.

Burgmann, S. & Janoske, U. 2021 Transmission and reduction of aerosols in classrooms using air purifier systems. *Phys. Fluids* **33**, 033321.

COMSOL Inc. 2017 CFD module user's guide. Available at: https://doc.comsol.com/5.4/doc/com.comsol.help.cfd/CFDModuleUsersGuide.pdf.

Dai, H. & Zhao, B. 2020 Association of the infection probability of COVID-19 with ventilation rates in confined spaces. *Build. Simul.* **13(6)**, 1321–1327.

Danckwerts, P. V. 1953 Continuous flow systems: Distribution of residence times. *Chem. Eng. Sci.* **2**, 1–13.

Dbouk, T., Roger, F. & Drikakis, D. 2021 Reducing indoor virus transmission using air purifiers. *Phys. Fluids* **33** (10), 103301.

De Oliveira, P. M., Mesquita, L. C. C., Gkantonas, S., Giusti, A. & Mastorakos, E. 2021 Evolution of spray and aerosol from respiratory releases: Theoretical estimates for insight on viral transmission. *Proc. Math. Phys. Eng. Sci.* **477** (2245), 20200584.

van Doremalen, N. *et al.* 2020 Aerosol and surface stability of SARS-CoV-2 as compared with SARS-CoV-1. *N. Engl. J. Med.* **382** (16), 1564–1567.

Foat, T., Drodge, J., Nally, J. & Parker, S. 2020 A relationship for the diffusion coefficient in eddy diffusion based indoor dispersion modelling. *Build. Environ.* **169**, 106591.

Gammaitoni, L. & Nucci, M. C. 1997 Using a mathematical model to evaluate the efficacy of TB control measures. *Emerg. Infect. Dis.* **3** (3), 335.

Günther, T. *et al.* 2020 SARS-CoV-2 outbreak investigation in a German meat processing plant. *EMBO Mol. Med.* **12**, e13296.

Guo, H., Morawska, L., He, C. & Gilbert, D. 2008 Impact of ventilation scenario on air exchange rates and on indoor particle number concentrations in an air-conditioned classroom. *Atmos. Environ.* **42** (4), 757–768.

Hallett, S., Toro, F. & Ashurst, J. V. 2020 Physiology, tidal volume. [Updated 2020 Jun 1]. In: StatPearls [Internet]. Treasure Island (FL): StatPearls Publishing; 2020 Jan-. Available from: https://www.ncbi.nlm.nih.gov/books/NBK482502/.

Ho, C. K. 2021 Modelling airborne transmission and ventilation impacts of a COVID-19 outbreak in a restaurant in Guangzhou, China. *Int. J. Comput. Fluid Dyn.* **35** (9), 708–726.

van Hooff, T., Blocken, B., Defraeye, T., Carmeliet, J. & Van Heijst, G. J. F. 2012 PIV

measurements and analysis of transitional flow in a reduced-scale model: Ventilation by a free plane jet with Coanda effect. *Build. Environ.* **56**, 301–313.

Kähler, C. J., Fuchs, T. & Hain, R. 2020 Can mobile indoor air cleaners effectively reduce an indirect risk of SARS-CoV-2 infection by aerosols? *Hg. v. Universität der Bundeswehr München. Strömungsmechanik und Aerodynamik* **18**.

Karlsson, E., Sjöstedt, A. & Håkansson, S. 1994 Can weak turbulence give high concentrations of carbon dioxide in baby cribs? *Atmos. Environ.* **28** (7), 1297–1300.

Lau, Z., Griffiths, I. M., English, A. & Kaouri, K. 2022 Predicting the spatio-temporal infection risk in indoor spaces using an efficient airborne transmission model. *Proc. Math. Phys. Eng. Sci.* **478** (2259), 20210383.

Lelieveld, J. *et al.* 2020 Model calculations of aerosol transmission and infection risk of COVID-19 in indoor environments. *Int. J. Environ. Res. Public Health* **17**, 8114.

Li, Y. *et al.* 2021 Probable airborne transmission of SARS-CoV-2 in a poorly ventilated restaurant. *Build. Environ.* **196**, 107788.

Lu, J. *et al.* 2020 COVID-19 outbreak associated with air conditioning in restaurant, Guangzhou, China, 2020. *Emerg. Infect. Dis.* **26** (7), 1628.

Menter, F. R. 1994 Two-equation eddy-viscosity turbulence models for engineering applications. *AIAA Journal* **32** (8), 1598–1605.

Miller, S. L. *et al.* 2021 Transmission of SARS-CoV-2 by inhalation of respiratory aerosol in the Skagit Valley Chorale superspreading event. *Indoor Air* **31**, 314–323.

Morawska, L. & Milton, D. K. 2020 It is time to address airborne transmission of COVID-19. *Clin. Infect. Dis.* **6**, ciaa939.

Narayanan, S. R. & Yang, S. 2021 Airborne transmission of virus-laden aerosols inside a music classroom: Effects of portable purifiers and aerosol injection rates. *Phys. Fluids* **33**, 033307.

Nightingale, F. 1860 *Notes on Nursing: What it is, and what it is not*. Harrison London.

Riley, E. C., Murphy, G. & Riley, R. L. 1978 Airborne spread of measles in a suburban elementary school. *Am. J. Epidemiol.* **107**, 421–432.

Shafaghi, A. H., Rokhsar, F. T. F., Koşar, A. & Ghorbani, M. 2020 On the effect of the respiratory droplet generation condition on COVID-19 transmission. *Fluids* **5** (3), 113.

Shao, S., Zhou, D., He, R., Li, J., Zou, S., Mallery, K., Kumar, S. & Yang, S. 2021 Risk assessment of airborne transmission of COVID-19 by asymptomatic individuals under different practical settings. *J. Aerosol Sci.* **151**, 105661.

Vernez, D., Schwarz, S., Sauvain, J.-J., Petignat, C. & Suarez, G. 2021 Probable aerosol transmission of SARS-CoV-2 in a poorly ventilated courtroom. *Indoor Air* **31** (6), 1776–1785.

Vuorinen, V. *et al.* 2020 Modelling aerosol transport and virus exposure with numerical simulations in relation to SARS-CoV-2 transmission by inhalation indoors. *Saf. Sci.* **130**, 104866.